



CHORUS

This is the accepted manuscript made available via CHORUS. The article has been published as:

Viscous fingering with partially miscible fluids

Xiaojing Fu, Luis Cueto-Felgueroso, and Ruben Juanes

Phys. Rev. Fluids **2**, 104001 — Published 9 October 2017

DOI: [10.1103/PhysRevFluids.2.104001](https://doi.org/10.1103/PhysRevFluids.2.104001)

Viscous fingering with partially miscible fluids

Xiaojing Fu¹, Luis Cueto-Felgueroso^{1,2} and Ruben Juanes¹

¹*Massachusetts Institute of Technology, 77 Massachusetts Ave.,*

Building 1, Cambridge, Massachusetts, MA 02139, USA

²*Technical University of Madrid, Calle del Profesor Aranguren 3, 28040 Madrid, Spain*

(Dated: September 24, 2017)

Viscous fingering—the fluid-mechanical instability that takes place when a low-viscosity fluid displaces a high-viscosity fluid—has traditionally been studied under either fully miscible or fully immiscible fluid systems. Here we study the impact of partial miscibility (a common occurrence in practice) on the fingering dynamics. Through a careful design of the thermodynamic free energy of a binary mixture, we develop a phase-field model of fluid-fluid displacements in a Hele-Shaw cell for the general case in which the two fluids have limited (but nonzero) solubility into one another. We show, by means of high-resolution numerical simulations, that partial miscibility exerts a powerful control on the degree of fingering: fluid dissolution hinders fingering while fluid exsolution enhances fingering. We also show that, as a result of the interplay between compositional exchange and the hydrodynamic pattern-forming process, stronger fingering promotes that the system approach thermodynamic equilibrium faster.

I. INTRODUCTION

21 When a less viscous fluid displaces a more viscous fluid, the contrast in viscosity desta-
 22 bilizes the fluid-fluid interface, leading to the formation of viscous fingers [1–3]. Fluid-fluid
 23 miscibility plays an important role in the fingering dynamics, and the fingering pattern can
 24 change appreciably based on the miscibility of two fluids. Thus, the subject is traditionally
 25 divided into *immiscible* and *miscible* viscous fingering. In both cases, it is viscous forces
 26 that drive the hydrodynamic instability. When two fluids are immiscible, surface tension
 27 stabilizes short-wavelength perturbations at the interface, allowing some proto-protrusions
 28 to spread readily, resulting in less ramified patterns [3–5]. When the two fluids are fully
 29 miscible, the absence of surface tension suggests a more intense fingering pattern, as demon-
 30 strated by experiments [3, 5–7] and simulations [8–12]. Nevertheless, without surface tension,
 31 complete suppression of the onset of miscible viscous fingering is possible under certain un-
 32 favorable viscosity contrast [6, 13] due to 3D effects. Beyond the onset regime, [7] has shown
 33 that molecular diffusion along the interface leads to shutdown of instability at late times
 34 during radial injections. Further, it has been suggested that Korteweg stresses and other
 35 non-equilibrium surface tension effects can act to stabilize miscible displacement [14–17].

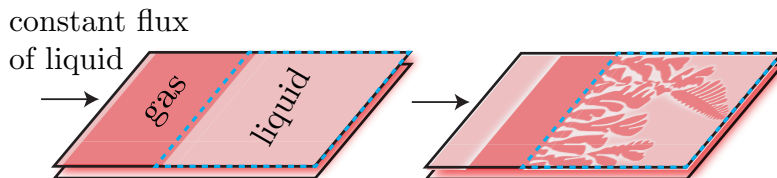
36 Despite the conventional categorization into fully immiscible and fully miscible, the mis-
 37 miscibility of two fluids can vary based on local conditions such as pressure and temperature
 38 [18]. Between the two extremes lie fluid pairs that are *partially miscible*, exhibiting lim-
 39 ited, but nonzero, solubility into each other. For such fluid pairs, compositional effects are
 40 introduced to two-phase problems where component exchange between phases occurs even
 41 in the presence of surface tension. This effect is relevant, for instance, during immiscible
 42 gas-in-oil injection for oil recovery where the gas and oil can become partially miscible under
 43 high pressure reservoir conditions, leading to swelling of the oil phase and enhanced recovery
 44 [19]. Under this context, the coupling of viscous fingering with thermodynamic effects could
 45 provide new insights to controlling of the viscous instability, which has received increased
 46 attention in recent studies [12, 20–24]. Additionally, addressing the role of compositional
 47 effects in low Reynolds number two-phase flows is also essential to our understanding of
 48 mixing in multiphase mixtures [25], biological cell assembly [26] and geologic sequestration
 49 of CO₂ [27].

50 Our current understanding of viscous fingering with partially miscible fluids is very lim-

51 ited. In an effort to address this gap, an experimental study on viscous fingering with
 52 partially miscible fluids is performed recently [28]. The experiments use a ternary system
 53 made of water, PEG and Na_2SO_4 to produce viscously-contrasting fluid pairs that are fully
 54 miscible, immiscible or partially miscible. The experiments provide an excellent illustration
 55 on how thermodynamic effects can exert a powerful control on hydrodynamic instabilities:
 56 as the fluid pairs transition from being immiscible to partially miscible, the authors observe
 57 that formation of droplets become more common than formation of fingers. The detailed
 58 mechanisms behind the droplets formation remain to be understood. On the modeling front,
 59 a recent study [29] investigated radial injection under different fluid miscibility conditions
 60 using a Darcy-Cahn-Hilliard model, where the fluid miscibility is prescribed through the
 61 design of a Cahn-Hilliard type free energy [30]. Though the model is limited in its ability
 62 to explore the truly partially miscible regime, where one would expect to see effects such as
 63 finger swelling due to supersaturation, the study provides a consistent comparison between
 64 immiscible and miscible viscous fingering to demonstrate the role of compositional effects
 65 in controlling the vigor of the instability. As presented in earlier work [7, 14], the study
 66 confirms that the degree of fingering instability, as measured by interface length, peaks at a
 67 transition time followed by a decay due to diffusive mixing at the interface for *miscible* sys-
 68 tems; in *immiscible* simulations, however, where surface tension is present and component
 69 diffusion is negligible, a decay in interfacial length is not observed [29].

70 In this work, we study the interplay between hydrodynamics and nonequilibrium com-
 71 positional effects in partially miscible systems. To develop new insights into the physics of
 72 a nonlinear hydrodynamic instability out of thermodynamic equilibrium, here we develop
 73 a 2D gap-averaged model, in the spirit of a large body of literature on Hele-Shaw flows
 74 for both miscible and immiscible fluids [8, 11, 12, 20, 22, 23, 31–36]. While a full 3D flow
 75 model might be desirable to eventually provide a more detailed description of the flow (as
 76 is the case for fully miscible [6, 13, 37–42] and fully immiscible systems [35, 36, 43–45]), it
 77 should build on the insights of the nonlinear analysis in 2D. We adopt a phase-field modeling
 78 approach, which has been successful at describing immiscible two-phase flow in Hele-Shaw
 79 geometry [35, 36, 46–52] and in porous media [53] and, more recently, the coarsening dynam-
 80 ics of partially miscible binary mixtures under viscous fingering [54]. Under the phase-field
 81 framework, the design of thermodynamic free energy allows us to readily incorporate partial
 82 miscibility into multiphase flow. In its minimal description, the free energy of a two-phase

83 two-component mixture follows the Cahn-Hilliard form [30], formulated as a functional of
 84 component concentration and its gradients. Under the Cahn-Hilliard framework, fluid phase
 85 is inferred from component concentration, and not independently described. This approach
 86 is successful in capturing the dynamics of binary mixtures with fast phase-transition time
 87 scale (e.g. immiscible fluids) [29, 55–60]. In contrast, our proposed model [54] allows fluid
 88 concentrations to evolve independently from the phase variable, in order to capture the
 89 essence of *partially miscible* systems, where components can exchange between the two
 90 phases at time scales comparable to that of flow. During injection, the evolution of the
 91 invading phase variable (e.g. volume fraction of the invading phase) is driven by viscous
 92 instability, accompanied by redistribution of composition between phases and phase trans-
 93 formations that are driven by chemical potentials. Capturing the duality of the dynamics
 94 requires having separate evolution equations for phase and concentration, and defining a
 95 free energy that is a function of both variables. Similar two-field formulations have been
 96 extensively adopted for the simulation of binary alloys solidification [61], but, thus far, not
 97 for interfacial flows with compositional effects. With this more general framework, we are
 98 able to investigate the two-way coupling between hydrodynamics (viscous fingering) and
 99 thermodynamics (compositional exchange between phases and phase transformation). We
 100 apply our model to the viscous fingering problem in a rectangular Hele-Shaw cell, where
 101 initially a gas band is surrounded by a liquid (Fig. 1, left). Gas fingers are then created
 102 by pushing the gas band leftwards with an imposed constant flux of the liquid phase of the
 103 same initial composition (Fig. 1, right).



105 FIG. 1. Displacement of a gas band through liquid phase in a Hele-Shaw cell: (a) initial set up (b)
 106 the displacement leads to viscous fingering due to viscosity contrast. Meanwhile, compositional
 107 exchange occurs along the fingering interface if the two fluids are out of thermodynamic equilibrium.
 108 For example, in this sample image, the liquid phase is initially supersaturated with respect to gas
 109 and will swell the gas fingers as they evolve (see Sec. IV A). The blue dashed box indicates the
 110 area of study in our discussions.

II. MATHEMATICAL MODEL

111

112 In our recent work [54], we propose a phase-field model of two-phase Darcy flow with two-
 113 component transport. Here we provide an extended and detailed description of the model
 114 and use it to study the problem described in Fig. 1. Without loss of generality, we focus on
 115 a binary mixture that is an analogy for a $\text{CO}_2(g)$ -water(l) system. The two fluids, denoted
 116 *gas* (g) and *liquid* (l), have different viscosities with $\mu_l > \mu_g$. Upon contact, they seek to
 117 reach compositional equilibrium through mutual component exchange. The result should be
 118 a gas phase that is rich in the primary component (e.g. CO_2) and a liquid that is rich in the
 119 secondary component (e.g. H_2O). We introduce two variables, defined pointwise, to describe
 120 the state of the binary mixture: the gas volume fraction, ϕ , is a nonconserved quantity due
 121 to dissolution/expansion of the gas phase; the molar fraction of CO_2 , c , is conservative in
 122 the entire domain. The model describes the evolution of ϕ and c when the binary mixture
 123 is subjected to hydrodynamic instabilities.

124

A. Phase-field modeling of two-phase Darcy flow with compositional effects

125 We introduce the following dimensional governing equations to describe incompressible,
 126 isothermal, two-phase flow with two-component transport in a Hele-Shaw cell, with a uniform
 127 gap thickness b :

$$\nabla \cdot \mathbf{u} = 0, \quad \mathbf{u} = -\frac{k}{\mu(\phi)} \nabla P, \quad (1)$$

$$\frac{\partial \phi}{\partial t} + \nabla \cdot (\mathbf{u}\phi) + \lambda^\phi \Psi_\phi = 0; \quad (2)$$

$$\frac{\partial c}{\partial t} + \nabla \cdot (\mathbf{u}c) - \nabla \cdot (\lambda^c \nabla \Psi_c) = 0. \quad (3)$$

128 Equations (1) are the continuity equation for an incompressible mixture and Darcy's law,
 129 where \mathbf{u} is the mixture velocity, P is a kinematic pressure, k is a constant permeability and
 130 μ is the mixture viscosity, assumed to follow an exponential dependence on phase fraction,
 131 $\mu(\phi) = \mu_g \exp(R(1 - \phi))$, where $R = \log(\mu_l/\mu_g)$ is the viscosity contrast.

132 In the context of phase-field modeling, we understand ϕ also as a phase variable, which
 133 takes a value of 1 in the gas and 0 in the liquid, and interpolates smoothly between the two

134 bulk phases over a well-resolved, diffuse numerical interface. Time evolution of ϕ simulates
 135 gas dissolution/exsolution [Eq. (2)], and can be considered a relaxation process towards a
 136 minimum of the free energy function of the system F [62]. The gradient towards minimiza-
 137 tion, obtained by taking the variational derivative of F with respect to ϕ , can be understood
 138 as a phase potential that drives phase-transformations:

$$\Psi_\phi \equiv \delta F / \delta \phi = \partial F / \partial \phi - \nabla \cdot [\partial F / \partial (\nabla \phi)]. \quad (4)$$

139 The dynamics of phase transformation [Eq. (2)] are formulated using Allen–Cahn dynam-
 140 ics [63]. The evolution of c is described by a nonlinear advection–diffusion equation [Eq. (13)],
 141 where the component diffusion is driven by gradients in chemical potentials, defined similarly
 142 to Eq. 4:

$$\Psi_c \equiv \delta F / \delta c = \partial F / \partial c - \nabla \cdot [\partial F / \partial (\nabla c)]. \quad (5)$$

143 In Eqs. (2) and (3), λ^ϕ and λ^c are mobilities for ϕ and c respectively. Here we assume that
 144 both mobilities are only a function of c :

$$\lambda^\phi b^2 = \lambda^c = \frac{D/\nu}{R_{\text{ideal}}T} (c(1-c) + 0.01), \quad (6)$$

145 where D is the diffusion coefficient, ν is the molar density, R_{ideal} is the ideal gas constant
 146 and T is temperature (assumed constant here). We define the characteristic composition
 147 mobility as:

$$\lambda_c = \frac{D/\nu}{R_{\text{ideal}}T}, \quad (7)$$

148 and the characteristic phase mobility as:

$$\lambda_c^\phi = \frac{D/\nu}{b^2 R_{\text{ideal}}T}. \quad (8)$$

149

B. Design of free energy

150 The free energy functional $F(\phi, c)$ plays a central role in the thermodynamic behavior
 151 of our binary mixture. Following the classical Cahn–Hilliard formulation for a binary sys-

152 tem [30], our F subsumes interfacial and bulk energy contributions:

$$\begin{aligned}
 F(\phi, c) = \int_V \left\{ \frac{1}{2} \epsilon_\phi^2 T (\nabla \phi)^2 + \frac{1}{2} \epsilon_c^2 T (\nabla c)^2 + \omega T W(\phi) \right. \\
 \left. + \omega_{\text{mix}} T [f_l(c)(1 - g(\phi)) + f_g(c)g(\phi)] \right\} dV.
 \end{aligned} \tag{9}$$

The first two terms in Eq. (9) capture the interfacial energy associated with phase and compositional boundaries. The characteristic interfacial energy per unit volume associated with ϕ and c are $\epsilon_\phi^2 T$ and $\epsilon_c^2 T$ respectively. The third term is the part of the bulk free energy responsible for phase separation, where $W(\phi) = \frac{1}{4} \phi^2 (1 - \phi)^2$ adopts the shape of a double-well, determining the two stable states of F : $\phi = 0$ or $\phi = 1$. Here, ω is the energy (per unit volume) associated with the double-well energy. The last term, known as the bulk mixing energy, is the part of the bulk free energy responsible for partially miscible behavior. We adopt a form for mixing energy that is commonly used in the field of binary alloy solidification [64], where the energy is an interpolation in ϕ between liquid and gas excess energies (f_l and f_g), which are functions of c only. Here, $\omega_{\text{mix}} T$ is the energy (per unit volume) associated with mixing. The interpolation function $g(\phi) = -\phi^2(2\phi - 3)$ satisfies that the system approaches the stable states $\phi = 0, 1$ with zero slope, which ensures positivity of the phase variable [64]. The excess free energy of each phase are due to compositional effects; here we adopt the Wilson model [65]:

$$\begin{aligned}
 f_l(c) &= c \log c + (1 - c) \log(1 - c) \\
 &\quad - c \log(c + \alpha_l(1 - c)) - (1 - c) \log(1 - c + \beta_l c), \\
 f_g(c) &= c \log c + (1 - c) \log(1 - c) \\
 &\quad - c \log(c + \alpha_g(1 - c)) - (1 - c) \log(1 - c + \beta_g c),
 \end{aligned} \tag{10}$$

153 where α_l , α_g , β_l and β_g are assigned parameters. The equilibrium concentrations within
 154 each phase are then obtained by the common tangent construction of f_l and f_g [66, 67]
 156 (Fig. 2). Note here that both $f_l(c)$ and $f_g(c)$ are dimensionless.

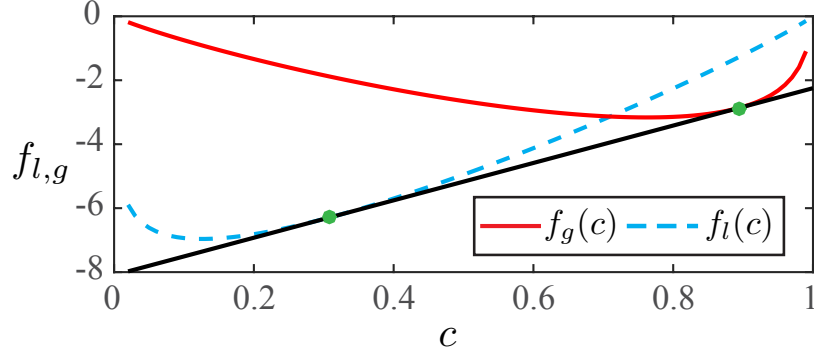


FIG. 2. Common tangent construction: here we assign the parameters in Eq. (10) as $\alpha_l = 2 \times 10^{-7}$, $\beta_l = 2 \times 10^4$, $\alpha_g = 200$, $\beta_g = 2 \times 10^{-4}$ so that the common tangent construction yields the equilibrium composition of the two fluids : $c_g^{\text{eq}} \approx 0.89$, $c_l^{\text{eq}} \approx 0.33$

157

C. Scaling analysis

158

159

160

161

162

163

We identify the following characteristic scales in our system: $\epsilon_\phi^2 T / b^2$ is the characteristic energy, b is the length scale, $t_c = b / u_c$ is the characteristic time with $u_c = (k_c \Delta p_c) / (\mu_g b)$, where k_c , Δp_c are the characteristic permeability and pressure drop respectively. Additionally, we introduce λ_c as the characteristic composition mobility [Eq. (7)] and λ_c^ϕ as the characteristic phase mobility [Eq. (8)]. In its dimensionless form, the system of equations reads:

$$\nabla \cdot \mathbf{u} = 0, \quad \mathbf{u} = -\frac{1}{\mu(\phi)} \nabla P, \quad (11)$$

$$\frac{\partial \phi}{\partial t} + \nabla \cdot (\mathbf{u} \phi) + \frac{1}{\text{Ca}} \lambda \Psi_\phi = 0, \quad (12)$$

$$\frac{\partial c}{\partial t} + \nabla \cdot (\mathbf{u} c) - \frac{1}{\text{Pe}} \nabla \cdot (\lambda \nabla \Psi_c) = 0. \quad (13)$$

164

165

where $\mu(\phi) = e^{R(1-\phi)}$ and $\lambda = 0.01 + c(1-c)$. The first dimensionless group, the capillary number Ca, sets the ratio between time scales associated with phase change and advection:

$$\text{Ca} = (u_c b) / (\lambda_c^\phi \epsilon_\phi^2 T), \quad (14)$$

166

167

where $\epsilon_\phi^2 T / b$ is the interfacial tension. We expect that Ca controls the characteristic length scale of the instability pattern, such that the characteristic length decreases with increasing

168 Ca [54]. The second dimensionless group, the Péclet number, sets the ratio between rate of
 169 advection and diffusion:

$$\text{Pe} = (u_c b) / (\lambda_c \epsilon_\phi^2 T). \quad (15)$$

170 Pe controls the rate of diffusion within a single phase, and therefore directly affects the rate of
 171 gas dissolution/exsolution. We expect that for large values of Pe, the finger morphology will
 172 approach that of an immiscible system. In dimensionless form, the free energy is described
 173 with three additional dimensionless groups:

$$F(\phi, c) = \int_V \left\{ \frac{1}{2} (\nabla \phi)^2 + \epsilon \frac{1}{2} (\nabla c)^2 + \frac{1}{\text{Ch}} W(\phi) + \frac{1}{\text{Ma}} [f_l(c)(1 - g(\phi)) + f_g(c)g(\phi)] \right\} dV. \quad (16)$$

174 We introduce the third dimensionless group as the ratio between the two energy scales
 175 associated with compositional and phase boundaries:

$$\epsilon = \epsilon_c^2 / \epsilon_\phi^2. \quad (17)$$

176 An increase in ϵ would mean that the numerical profile of concentration (c) becomes sharper
 177 and the numerical profile of phases (ϕ) becomes smoother. The fourth group is the Cahn
 178 number, which controls the thickness of the numerical interface:

$$\text{Ch} = (\epsilon_\phi^2 / b^2) / \omega. \quad (18)$$

179 A larger Ch would require more grid points to resolve the fluid-fluid interface. Phenomeno-
 180 logically, a larger Ch also corresponds to a system with larger surface tension. Finally,
 181 we define a solutal Marangoni number, which sets the ratio between interfacial energy and
 182 mixing energy:

$$\text{Ma} = (\epsilon_\phi^2 / b^2) / \omega_{\text{mix}}. \quad (19)$$

183 As Ma increases, the system becomes dominated by interfacial effects and we expect non-
 184 equilibrium thermodynamics to play a weaker role in the pattern forming process.

185 III. PROBLEM SETUP AND NUMERICAL METHODS

186 We conduct high-resolution numerical simulations of our model for the problem described
 187 in Fig. 1, in which we displace a band of less viscous gas through the more viscous ambi-
 188 ent liquid under a constant flux of liquid of the same initial composition. Our simulations
 189 are on a domain of size 200×80 ($L_x \times L_y$) and parameter values $\text{Ch}=1/2000$, $\text{Ma}=1/200$
 190 and $\epsilon=200$ (and parameters of the Wilson model given in Fig. 2). We perform a straight-
 191 forward calculation of Ca and Pe in order to mimic an experimental fluid pairs analogous
 192 to water and methane gas (weakly soluble in water). We approximate the typical injection
 193 rate in a rectilinear geometry to be $U = 1.9 \times 10^{-3} \text{cm/s}$, based on the values reported in
 194 [44]. The surface tension is take as that of water and air at room temperature: $\epsilon_\phi^2 T/b = 72$
 195 dyn/cm . The diffusion coefficient of gas in water at 25°C is taken from [68] as $D = 2 \times 10^{-5}$
 196 cm^2/s . The molar density of pure water is about 0.056mol/cm^3 , and that of gas is about
 197 0.00005mol/cm^3 . Here we take an intermediate value of 0.01mol/cm^3 for ν . Based on
 198 these values, we calculate that $\lambda_c^\phi = 1.29 \times 10^{-5} \text{cm}^3/(J \cdot \text{s})$ and $\lambda_c = 8.1 \times 10^{-7} \text{cm}^5/(J \cdot \text{s})$.
 199 The key dimensionless parameters in our system are computed as: $\text{Ca} = U/(\lambda_c^\phi \gamma) \approx 2$ and
 200 $\text{Pe} = U/\lambda_c \gamma \approx 32$.

201 We are interested in exploring the coupling between hydrodynamic instabilities and ther-
 202 modynamic effects. Consequentially, we focus on two parameters, each of which controls one
 203 aspect of the coupling: (a) the viscosity contrast R between the two fluids and (b) the initial
 204 composition of the liquid phase c_l^0 . The parameter R is chosen here to be $R = 0, 1, 2, 3, 4$
 205 and 5 , where the gas phase is always less (or equally) viscous than the liquid. The value
 206 of c_l^0 determines the thermodynamic response of the two fluids when interacting, where
 207 three scenarios may occur: (i) the gas dissolves, transferring CO_2 into the liquid; (i) the
 208 gas and liquid are at equilibrium, no component exchange occurs; or (iii) the gas expands
 209 in volume by exsolving CO_2 from the liquid. As shown in Fig. 2, the common tangent con-
 210 struction of the bulk free energies yields the equilibrium composition of the two fluids as:
 211 $c_g^{\text{eq}} \approx 0.89, c_l^{\text{eq}} \approx 0.33$. Instructed by this calculation, we can re-create the three scenarios
 212 by setting the defending liquid to be initially (at $t = 0$):

213 (a) *undersaturated* with respect to the gas phase: $c_l^0 = 0.05 < c_l^{\text{eq}}$;

214 (b) *near-saturated* with respect to the gas phase: $c_l^0 = 0.33 \approx c_l^{\text{eq}}$;

215 (c) *supersaturated* with respect to the gas phase: $c_l^0 = 0.5 > c_l^{\text{eq}}$.

216 In all the simulations performed, we only vary R and c_l^0 while all other parameters are
 217 unchanged. We initialize the gas phase with a composition that is close to equilibrium
 218 values: $c_g^0 = 0.89 \approx c_g^{\text{eq}}$. Further, all simulations start with the same initial configuration in
 219 ϕ (as shown in Fig. 1 left):

$$\phi_0 = \begin{cases} 1, & \text{if } 0.05L_x \leq x \leq 0.4L_x \\ 0, & \text{otherwise} \end{cases} \quad (20)$$

220 The initial concentration field c_0 is computed as an affine mapping from ϕ_0 :

$$c_0 = (c_l^0 - c_g^0)(1 - \phi_0) + c_g^0. \quad (21)$$

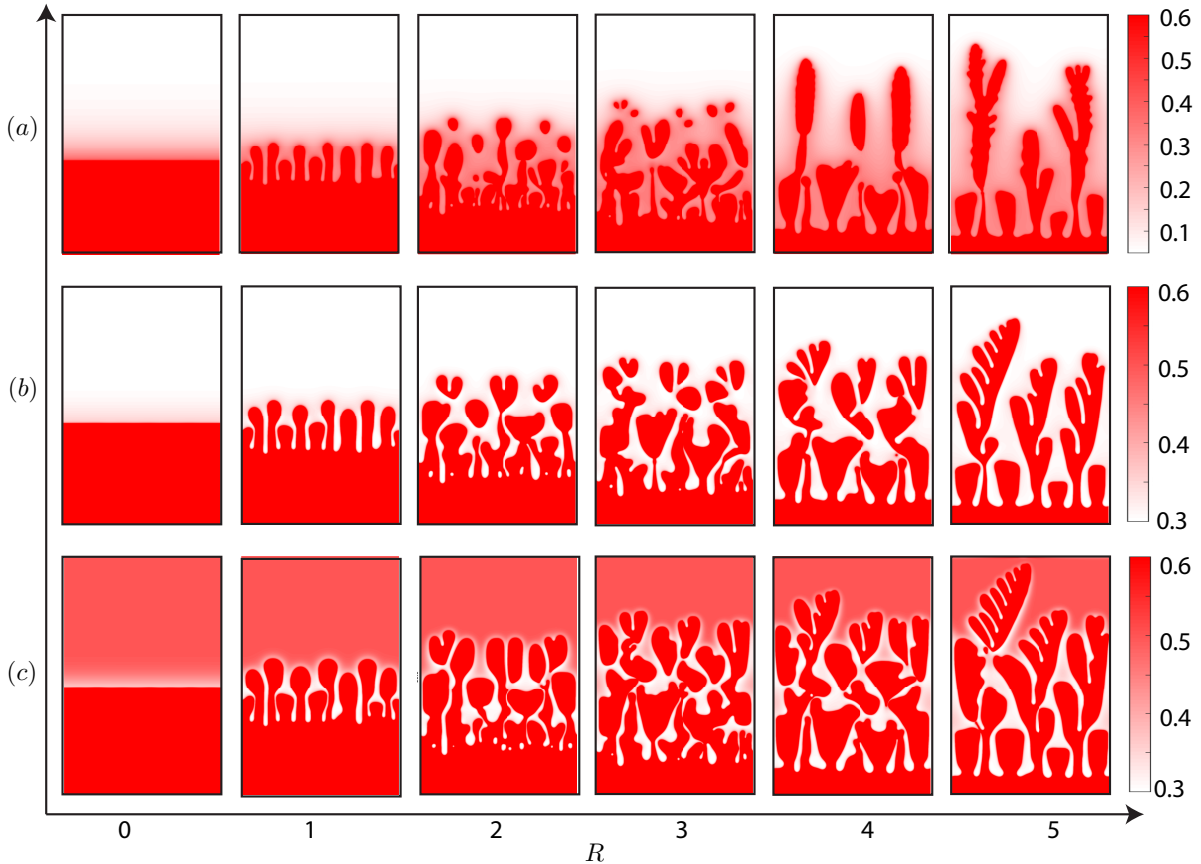
221 We solve Eqs. (11)–(13) sequentially. We first obtain the pressure and velocity using a
 222 finite volume method with a two-point flux approximation. Next we update c and ϕ using a
 223 Fourier pseudo-spectral discretization and using a biharmonic-modified time stepping [69].
 224 The domain is discretized with 2560×1024 ($N_x \times N_y$) points. The boundary conditions
 225 are periodic, but we show results only in a window of the simulation domain ($80 \leq L_x \leq$
 226 200 , indicated as the blue dashed box in Fig. 1) unaffected by the boundaries during the
 227 simulation period reported (that is, until the fingers reach the right boundary).

228 IV. RESULTS

229 A. Fingering pattern under the influence of gas dissolution and exsolution

230 We present a summary of the final displacement pattern (in c) in a c_l^0 – R phase diagram
 231 in Fig. 3. The middle row of the phase diagram corresponds to a displacement scenario
 232 where the two fluids are near-saturated, analogous to immiscible displacement [4, 70]. In
 233 this regime, viscosity ratio is understood as the control parameter for large scale structure of
 234 the pattern [2, 71]. With this series of simulations, we recover the classic features of immis-
 235 cible viscous fingering: shielding, spreading and tip-splitting [2], as well as side-branching,
 236 merging, pinchoff of fingers, and entrapment of the defending phase towards the injection

side [72, 73]. The rest of the phase diagram (top and bottom rows) illustrates the effects of
 gas dissolution/exsolution on the displacement patterns.



239

FIG. 3. The coupling between different viscosity contrast and compositional effects lead to a rich
 set of viscous fingering patterns. Here we show snapshots of c at $t = 50$ for six different R values
 (across each row). Each of the three rows correspond to different c_l^0 values: defending liquid is (a)
 undersaturated ($c_l^0 = 0.05$); (b) near-saturated ($c_l^0 = 0.33$) and (c) oversaturated ($c_l^0 = 0.5$). Note
 that the colormap differs between each row to reveal the detailed structures in the concentration
 field.

In the top row, the defending liquid is undersaturated with respect to the gas. Upon
 contact, the gas volume dissolves locally to replenish the CO_2 concentration level in the
 ambient liquid. This dissolution process hinders the growth of young fingers, or proto-
 protrusions, that form along the sides of dominant fingers. By immediately stripping away
 any gas accumulation that fuels the growth of instability, the dissolution process inhibits
 proto-protrusions developing into mature fingers. As a result, it has significantly weakened
 development of side branches as well as the shielding and merging processes. The dissolution
 effect is most active towards the front of the invasion, where the gas phase is persistently

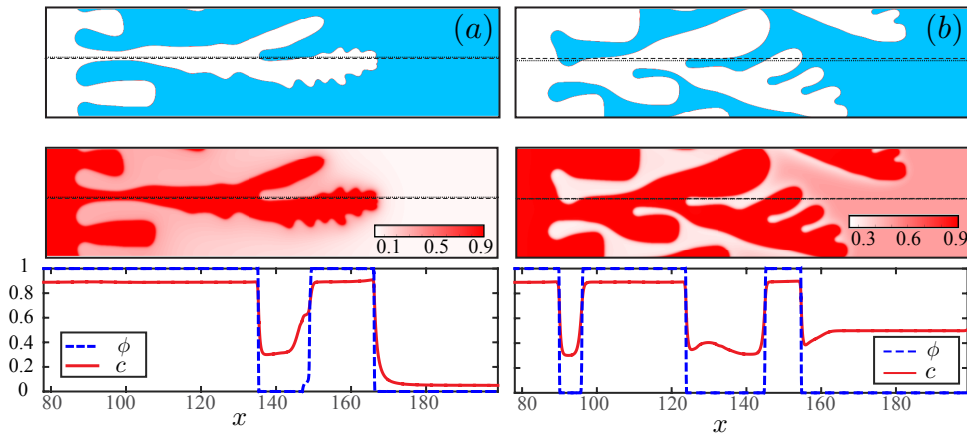
254 met with undersaturated liquid. Under this effect, the un-bifurcated fingers appear slimmer
 255 ($R = 1$), and we observe disconnected droplets that become rounded due to dissolution for
 256 intermediate viscosity contrast ($R = 2, 3$); for larger viscosity contrast ($R = 4, 5$), we
 257 observe “bald” dominant fingers that lack active side branches.

258 An important distinction between partially and fully miscible fluids pair is the direction
 259 of component diffusion. In a fully miscible system, molecular diffusion of the components
 260 follow the direction of positive concentration gradient. In the case of partially miscible fluids,
 261 however, component diffusion is directed in the direction of chemical potential gradient,
 262 which can sometimes be the reverse of the concentration gradient. Such is the case when
 263 the gas phase is exposed to an oversaturated liquid (bottom row of the phase diagram),
 264 where the invading fingers swell by exsolving the excess CO_2 from the liquid, against the
 265 direction of concentration gradient. Exsolution into the gas phase increases the volume of
 266 gas (ϕ) and thus promotes instability in the system as it expands the radius of invading
 267 front for tip-splitting [4]. This results in an enhanced shielding and merging effect and more
 268 prominent side branches. Such promotion of instability is observed across all values of R
 269 where fingering occurs, and the effect is most apparent for $R = 4, 5$. In addition, the fingers
 270 also appear larger overall in comparison to the middle row.

271 B. The coupling between ϕ and c

272 We illustrate the fingering pattern using the c -field in Fig. 3; however, it is important to
 273 note that both ϕ and c are independently solved using separate evolution equations in our
 274 model. To demonstrate this, Fig. 4 shows snapshots of 1D cross section profiles of both ϕ and
 275 c side-by-side for $R = 5$ with *unsaturated* (left) and *oversaturated* (right) defending fluid.
 276 From this we observe that both ϕ and c , although independently solved, follow each other
 277 closely. The pattern in c emulates that of ϕ , although c provides more details on component
 278 distribution within each phase. There are, however, fundamental differences in how these
 279 two variables behave under their own evolution equation. The 1D profile of ϕ (Fig. 4 bottom,
 280 dashed blue line) is continuous but compact—a feature of immiscible invasion under diffuse-
 281 interface descriptions. Meanwhile the 1D profile of c (Fig. 4 bottom, solid red line) exhibits
 282 a diffuse profile that is inherent to diffusive component transport. The coupling between ϕ
 283 and c is not merely a modeling construct: rather, it provides compositional details of the

284 two-phase system that either variable alone would not be able to reveal. This is further
 285 discussed in Sec. IV E.



286

287 FIG. 4. Defending fluid is (a) undersaturated or (b) supersaturated. Top: snapshots of ϕ at $t = 46$.
 288 Middle: snapshots of c at $t = 46$. Bottom: horizontal transects of ϕ (dashed) and c (solid)
 289 along the dashed lines indicated in the 2D plots in the top and middle rows. Note that regions
 290 where $c \approx 0.33$ indicate area in which local thermodynamic equilibrium is in place.

291

C. Thermodynamic control on the degree of fingering

292 Thermodynamic effects such as chemical reactions can lead to a myriad of interesting be-
 293 haviors when coupled with hydrodynamic instabilities [24, 74–77]. In this work, we explore
 294 such coupling in the form of thermodynamics-driven phase transformation that leads to fin-
 295 ger dissolution and exsolution during viscous fingering. The coupling can be of particular
 296 interest in the context of controlling of the viscous instability, which has received increased
 297 attention in recent studies [12, 20–24]. Proposed mechanisms include use of chemical reac-
 298 tions [24], alternating injections [12], control of injection rate [20, 78], imposing a gradient
 299 in flow pathway [22, 79], or confining the flow by elastic membranes [23].

300 In Section IV A, we demonstrate qualitatively that thermodynamic-driven phase transfor-
 301 mations, resulting in fluid dissolution or exsolution, can hinder or enhance viscous fingering
 302 instabilities beyond onset regime. Here we quantify such effect by inferring the degree of
 303 fingering with direct measurement of the total interfacial length generated by the instabil-
 304 ity, using image segmentation (see examples in Fig. 5 insets). The interfacial length of the
 305 fingering front, \mathcal{L} , is scaled by the transversal domain length, $L_y = 80$, so that initially
 306 $\mathcal{L}/L_y = 1$ and will increase as fingers form and grow (Fig. 5). When $R = 0$, $\mathcal{L}/L_y = 1$

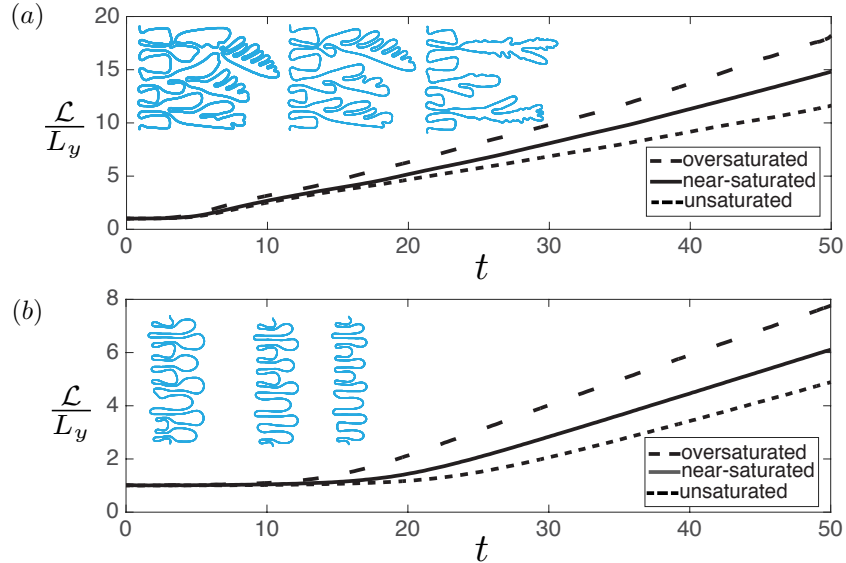


FIG. 5. Normalized interfacial length, \mathcal{L}/L_y , as a function of time for three compositional scenarios with (a) $R = 5$ and (b) $R = 1$. In both plots, colored insets show the traced outline of the fingering front at $t = 50$ for oversaturated, near-saturated and unsaturated defending liquid (left to right).

307 for the entirety of the simulation. In Fig. 5, we show the evolution of \mathcal{L}/L_y under $R = 1$
 308 (bottom) and $R = 5$ (top) for all three compositional scenarios. The degree of fingering
 309 persistently increases under all scenarios; the instability is not suppressed due to gas dis-
 310 solution. However, compared to the second scenario (the immiscible analog, solid lines),
 311 the interfacial growth is slowed down under gas dissolution (short dashed line), indicating
 312 weakening of the instability; on the other hand, the growth is significant enhanced under
 313 finger swelling (long dashed line), indicating promotion of the instability.

314 The insets in Fig. 5(b) also illustrates a greater finger competition for the oversaturated
 315 case. This is due to the fact that under an oversaturated scenario, gas exsolution leads to
 316 finger swelling and a space-filling competition that promotes of some fingers while suppressing
 317 some others. This enhanced competition is not observed for the unsaturated cases at $R = 1$.

318 D. Impact of viscous fingering on the rate of gas dissolution/exsolution

319 The total gas volume fraction in the system should decrease due to gas dissolution or
 320 increase due to gas exsolution. In other words, the amount of gas volume change in the
 321 domain is a global measure that reflects how much the system has progressed towards
 322 thermodynamic equilibrium.

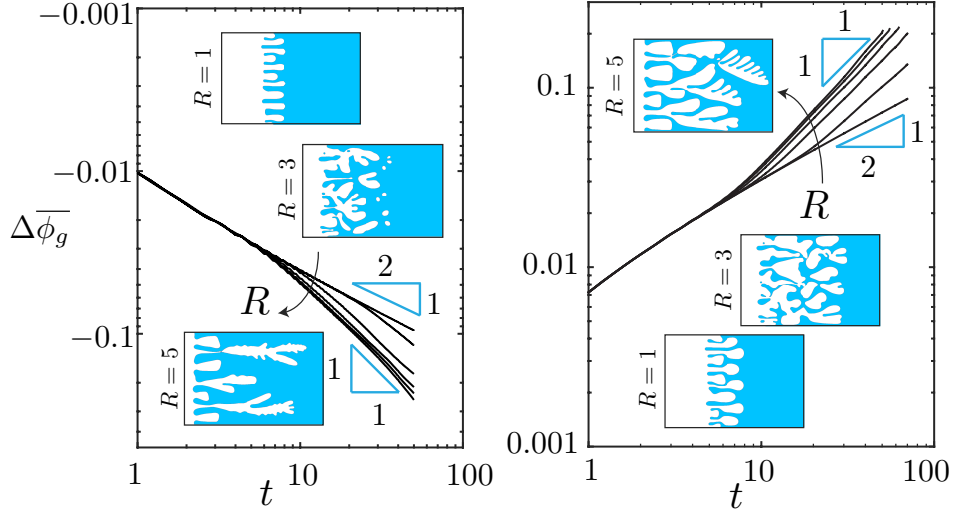


FIG. 6. $\Delta\bar{\phi}_g(t)$ for $R = 0, 1, 2, 3, 4, 5$ (arrows indicating increasing order) when the defending phase is undersaturated (left) and supersaturated (right). The insets in both plots show snapshots of ϕ at $t = 50$ for the different values of R .

323 Locally, the reduction or increase in gas volume is a direct consequence of component
 324 exchange across the phase-phase boundary. We expect that hydrodynamic instability will
 325 play an important role in this process because phase transformations take place at the
 326 invasion front where the two fluids are out-of-equilibrium, and viscous fingering deforms and
 327 lengthens such front.

328 Here, we define the change in gas volume fraction across the whole domain over time as:

$$\Delta\bar{\phi}_g(t) = \frac{\iint \phi(t) dx dy - \iint \phi_0 dx dy}{\iint \phi_0 dx dy}. \quad (22)$$

329 In Fig. 6, we show $\Delta\bar{\phi}_g(t)$ for different values of R when the defending fluid is undersaturated
 330 (left) and supersaturated (right). When no viscosity contrast is present ($R = 0$), the invasion
 331 front remains stable and phase transformation is limited by the rate at which CO_2 diffuses
 332 in the liquid phase in order to be transported away or towards the gas phase. This explains
 333 $|\Delta\bar{\phi}_g| \sim t^{1/2}$ for $R = 0$ in both composition scenarios. In the presence of the hydrodynamic
 334 instability ($R > 0$), the invasion-front deformation provides more interfacial area over which
 335 the two fluids can equilibrate. This mass-transfer enhancement is clearly shown in the scaling
 336 $|\Delta\bar{\phi}_g| \sim t^1$, observed for $R = 2, 3, 4, 5$.

337 E. Heterogeneity in phase compositions

338 While gas volume fraction is a measure of how the system progresses towards its ther-
 339 modynamic equilibrium globally, here we show that progress towards equilibrium can be
 340 very heterogeneous within the domain. To do this, we track the liquid phase concentration,
 341 computed pointwise as:

$$c_l(x, y) = (1 - \phi(x, y))c(x, y). \quad (23)$$

342 We introduce $\bar{c}_{ly}(x)$ as the y -averaged liquid phase concentration along the x -axis. If a
 343 thermodynamic equilibrium is reached locally, $\bar{c}_{ly} \approx c_l^{\text{eq}}$ at that point; otherwise, \bar{c}_{ly} should
 344 be larger or smaller than c_l^{eq} . In Fig. 7 (left column), we plot $\bar{c}_{ly}(x)$ at six different times
 345 with $R = 5$ for undersaturated [Fig. 7(a)] and supersaturated [Fig. 7(b)] defending liquid.
 346 The shaded red region indicates *metastability*, where the system is close to thermodynamic
 347 equilibrium (red dashed lines Fig. 7). From this, we observe that the system reaches
 348 metastability towards the roots of the fingers, where two fluids have more time to equilibrate.
 349 Towards the fingering front, the fluid-fluid interface is newly created, leaving little time for
 350 component exchange to occur; therefore, the liquid composition appears to be far away from
 351 thermodynamic equilibrium at the fingering front. The spatial heterogeneity in the phase
 352 compositions and consequently in the thermodynamic equilibrium state between the fluids
 353 has implications on the pattern forming process: towards the roots of the fingers, where the
 354 system has established a thermodynamic equilibrium earlier, the fingering morphology is no
 355 longer subject to dissolution/exsolution effects; towards the invasion front, freshly created
 356 fingers are subject to constant shrinkage/expansion due to gas dissolution/exsolution.

357 F. Fingering pattern as controlled by Ch and Ma

358 The Cahn number (Ch) controls the effective surface tension between the two fluids. As
 359 Ch increases, the system experiences increasing surface tension. Here we verify this effect by
 360 simulating viscous fingering at four different values of Ch at a fixed $\text{Ma} = 1/200$ (all other
 361 parameters are kept the same as introduced in Sec. III). The results as shown in Fig. 8
 362 demonstrate that as Ch increases from left to right, an increasing surface tension results in
 363 more prominent finger pinch-off.

364 The solutal Marangoni number (Ma) controls the thermodynamic forcing that leads to

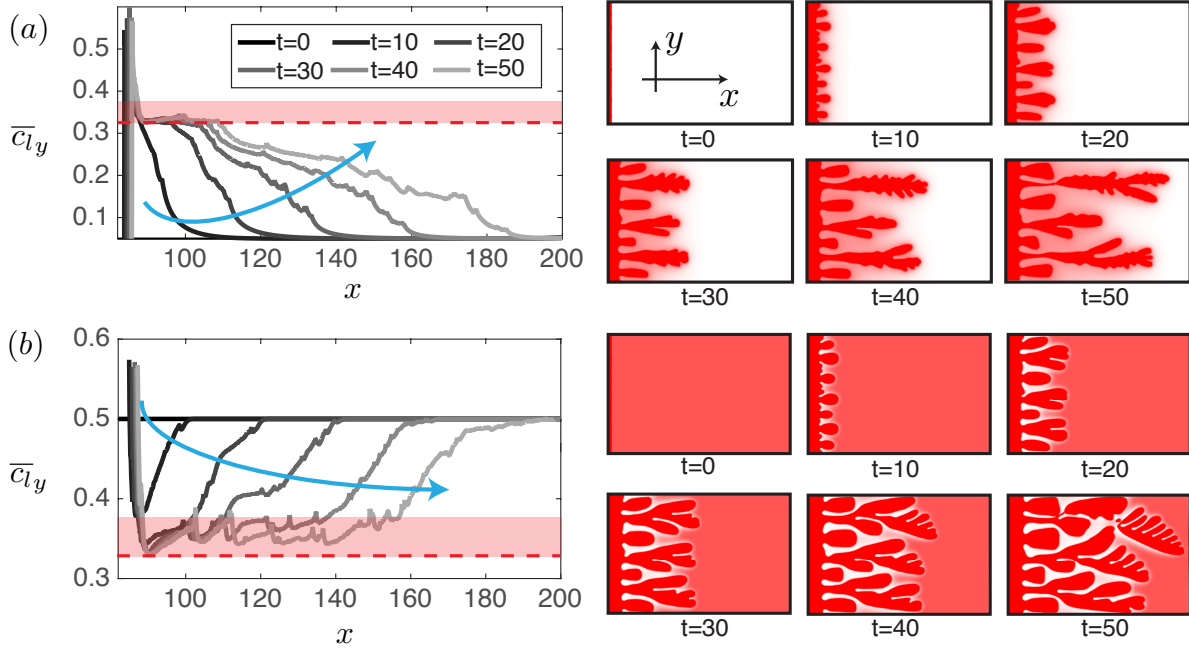


FIG. 7. (Left) $\bar{c}_{ly}(x)$ at $t = 0, 10, 20, 30, 40$ and 50 . Blue arrow indicates direction of time. Red dashed line indicates thermodynamic equilibrium: $c_l^{\text{eq}} \approx 0.33$. Red shaded area indicates metastability. (Right) snapshots of c for the corresponding times. The defending liquid is initially undersaturated in (a) and supersaturated in (b), and all simulations correspond to $R = 5$.

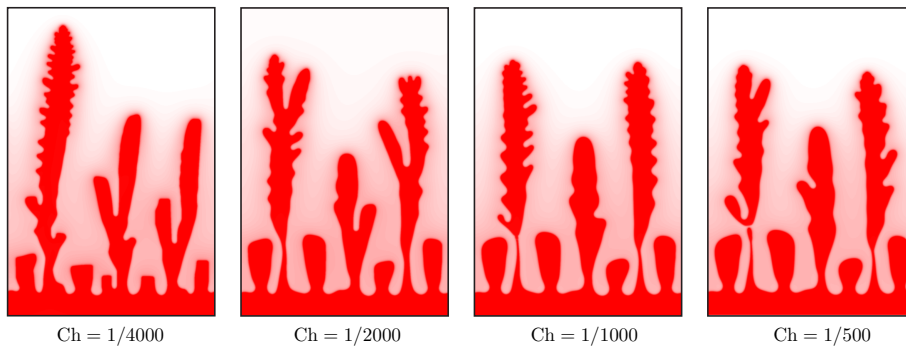


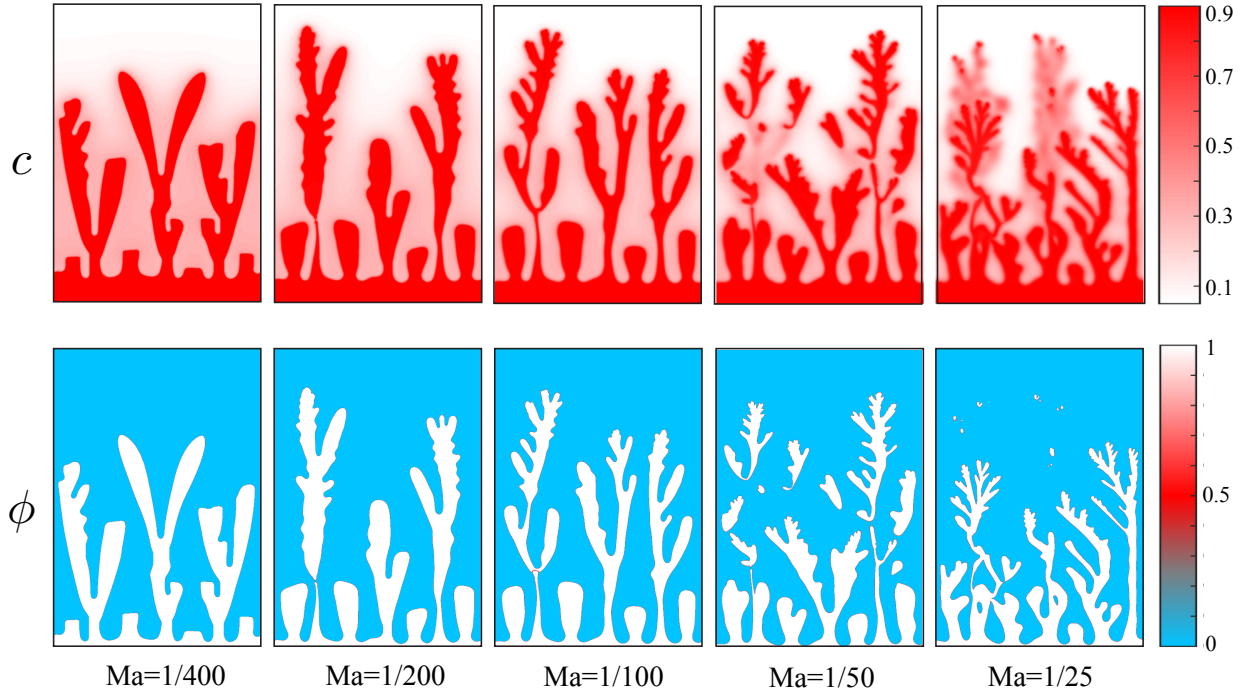
FIG. 8. Impact of Cahn number at $Ma = 1/200$ and other parameters kept the same as in Sec. III. We simulate for four values of Ch differing by a factor of two each. Shown here are snapshots of c at $t = 40$. The colormap range is $[0.05, 0.9]$ for all figures.

365 partial miscibility. It appears as a coefficient of the chemical potential, which is defined as:

$$\Psi_c = \epsilon \nabla^2 c + \frac{1}{Ma} [f'_l(c)(1 - g(\phi)) + f'_g(c)g(\phi)]. \quad (24)$$

366 Although Ma does not change the compositional equilibrium, one can treat $1/Ma$ as a
 367 kinetic rate coefficient that drives component diffusion within each phase. Such diffusion is

368 proportional to the gradient in Ψ_c and will diminish as the system approaches equilibrium
 369 (the expression multiplied by $1/\text{Ma}$ will be zero at equilibrium). As Ma increases, the rate
 370 of diffusion decreases within each phase and the system takes longer to reach compositional
 371 equilibrium. This effect is confirmed by Fig. 9, where we see that as Ma increases from
 372 left to right, the liquid phase composition is more heterogeneous and farther away from
 373 equilibrium (supersaturated in many regions for $\text{Ma} = 1/50$ and $1/25$).



374

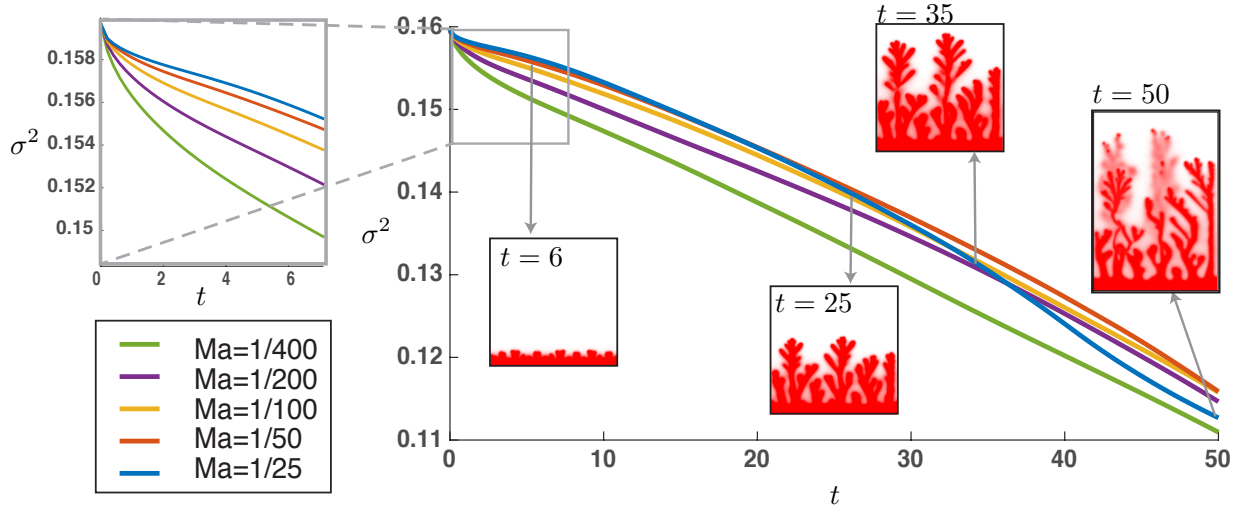
375 FIG. 9. Impact of solutal Marangoni number at $\text{Ch} = 1/2000$ and other parameters kept the same
 376 as in Sec. III. We simulate for five values of Ma differing by a factor of two each. Shown here are
 377 snapshots of c (top) and ϕ (bottom) at $t = 50$.

378 It is also important to note that a decrease in $1/\text{Ma}$ also indirectly promotes the strength
 379 of surface tension in the system. This is due to the structure of the free energy design
 380 [Eq. (16)]. As a result, an increase in Ma indicates an increase in surface tension, allowing the
 381 system to favor more pinch-off and tip-splitting events (Fig. 9). Such nonlinear interactions
 382 between compositional effects and fluid instability lead to interesting dynamics in fluid
 383 mixing. Here, we use the variance of the concentration field to measure fluid mixing:

$$\sigma^2 = \langle c^2 \rangle - \langle c \rangle^2. \quad (25)$$

384 In Fig. 10, we study the effect of Ma on fluid mixing by analyzing the temporal dynamics

385 of σ^2 from the set of simulations shown in Fig. 9. We conclude that the rate of mixing
 386 is initially enhanced by smaller Ma (enlarged figure to the left), which is consistent with
 387 the implication from Eq. (24). However, as a result of nonlinear coupling between fingering
 388 instability and dissolution effects, a larger Ma (e.g. $\text{Ma} = 1/25$) produces significantly more
 389 tip-splitting and pinch-off events, which results in the creation of more interfacial area and
 390 faster mixing at later times (Fig. 10, $t > 20$).



391

392 FIG. 10. Concentration variance σ^2 as a function of time for different values of Ma. The enlarged
 393 portion on the left corresponds to the early time regime when the fluid interface has not been
 394 significantly destabilized. The insets in the main figure correspond to snapshots of c for the
 395 $\text{Ma} = 1/25$ simulation.

396

G. Fingering pattern with decreasing miscibility gap

397

The miscibility gap of a fluids pair is defined here as the difference in compositions between
 398 the two fluids once they reach compositional equilibrium: $c_g^{\text{eq}} - c_l^{\text{eq}}$. In our current model, the
 399 miscibility gap is determined solely by the description of the bulk mixing energy functions
 400 $f_l(c)$ and $f_g(c)$. By changing the parameter values in Eq. (10), we explore the ability of our
 401 model framework to describe fluid pairs with different levels of partial miscibility. We stress
 402 here that the miscibility gap is determined solely by the shape of the bulk mixing energy
 403 curves $f_l(c)$ and $f_g(c)$; tuning the parameters Ma, Ch, ϵ , Pe and Ca will only change the
 404 dynamics as the system approaches equilibrium.

405

In Fig. 11, we explore the pattern-forming dynamics as we inject fluid pairs with a

406 different miscibility gap. This is done by tuning the parameters (α_l , α_g , β_l and β_g) in the
 407 bulk mixing energy curves of each phase [Eq. (10)]. As we close the miscibility gap (top to
 408 bottom), we also change the initial condition in concentration so that the liquid phase is
 409 always undersaturated and the gas phase is at-saturation. Specifically,

- 410 • The top row corresponds to the majority of the simulations discussed in this work,
 411 where $\alpha_l = 2 \times 10^{-7}$, $\beta_l = 2 \times 10^4$, $\alpha_g = 200$, $\beta_g = 2 \times 10^{-4}$ so that the common tangent
 412 construction yields the equilibrium composition of the two fluids: $c_g^{\text{eq}} \approx 0.89$, $c_l^{\text{eq}} \approx$
 413 0.33 ;
- 414 • The middle row corresponds to $\alpha_l = 20$, $\beta_l = 200$, $\alpha_g = 200$, $\beta_g = 20$ so that the
 415 common tangent construction yields the equilibrium composition of the two fluids:
 416 $c_g^{\text{eq}} \approx 0.65$, $c_l^{\text{eq}} \approx 0.35$;
- 417 • The bottom row corresponds to $\alpha_l = 100$, $\beta_l = 200$, $\alpha_g = 200$, $\beta_g = 100$ so that the
 418 common tangent construction yields the equilibrium composition of the two fluids:
 419 $c_g^{\text{eq}} \approx 0.55$, $c_l^{\text{eq}} \approx 0.45$.

420 We keep all the other parameters the same as introduced in Sec. III. In Fig. 11, we
 421 observe that even as the miscibility gap narrows (approaching the fully miscible limit), where
 422 one might expect a transition to a miscible viscous fingering pattern [11], the system always
 423 exhibits the effect of interfacial tension and the fingering pattern resembles that of immiscible
 424 displacement. This effect is due to our simplified description of mixture viscosity and surface
 425 tension. Currently, viscosity in our model is a function of ϕ only, and the effective surface
 426 tension is independent of fluid composition. Incorporating a more sophisticated design of
 427 viscosity as a function of both ϕ and c and a concentration-dependent surface tension term
 428 may allow our model to capture more accurately the transitions towards the fully miscible
 429 limit. Nevertheless, the model is robust in capturing the correct thermodynamics, where the
 430 fluids arrive at their respective equilibrium compositions as predicted by the bulk mixing
 431 energy curves in all three cases.

432 V. CONCLUSIONS

433 In this paper, we study viscous fingering with partially miscible fluids. We introduce a
 434 phase-field model to describe two-phase two-component flow and transport in a Hele-Shaw

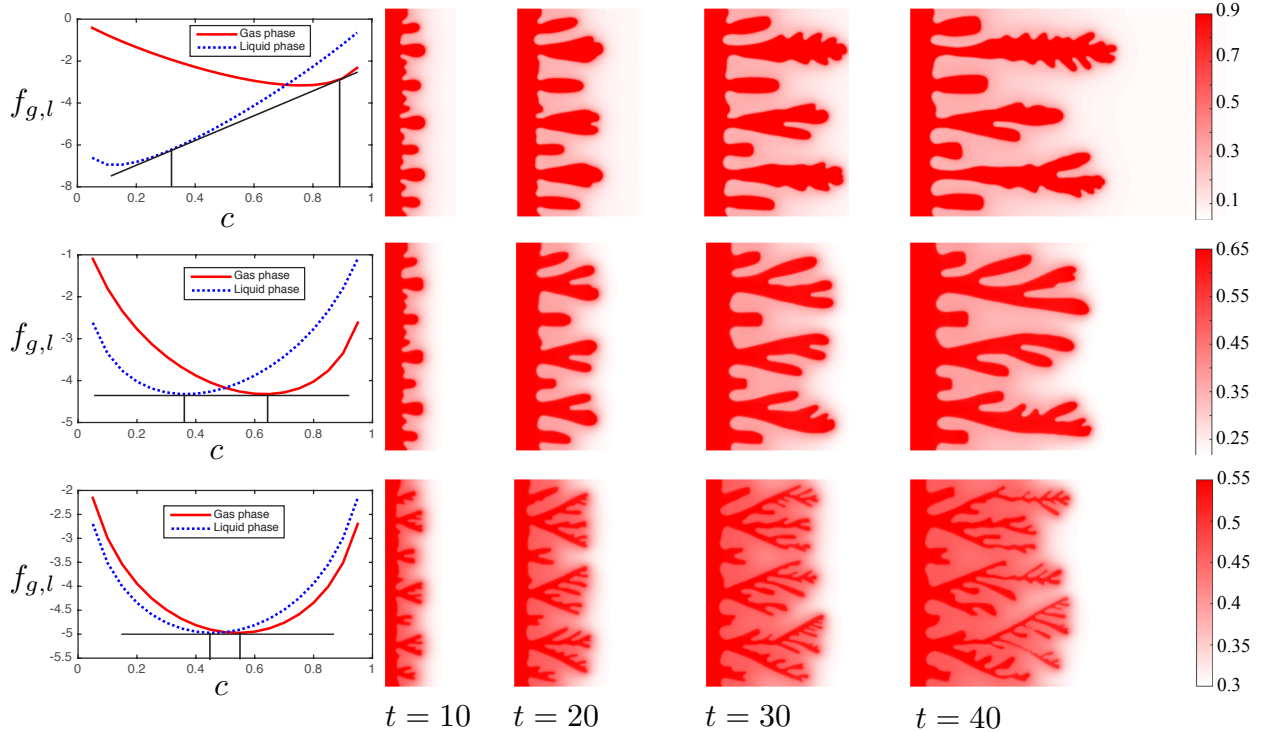


FIG. 11. Impact of miscibility gap in the bulk mixing energy curves. (Left): $f_l(c)$ and $f_g(c)$ and their common tangent constructions. (Right): snapshots of c from simulations using the bulk mixing energy described in the left column. Note that the colormap ranges are different and correspond to the initial composition (slightly wider than miscibility gap).

435 cell. We present high-resolution numerical simulations of the model applied to the viscous
 436 fingering problem for various viscosity contrasts and different initial fluid compositions.
 437 From the perspective of pattern formation, our results demonstrate that fluid dissolution or
 438 exsolution due to partial miscibility can hinder or enhance viscous fingering, respectively.
 439 This is shown by both directly visualizing the fingering pattern (Sec. IV A), and also by
 440 quantifying the degree of fingering through the measure of interfacial length (Sec. IV C).

441 Conversely, we also explore how the pattern forming process can impact the rate at which
 442 the two fluids reach compositional equilibrium. By measuring globally the amount of gas
 443 dissolution/expansion from component mass transfer, we show that the increase in degree of
 444 fingering—and associated increase in interfacial length—is directly linked to a faster rate of
 445 thermodynamic equilibration (Sec. IV D). By measuring locally the degree of equilibrium,
 446 we show that equilibrium is reached earlier towards the roots of the fingers, where the two
 447 fluids have more time to exchange components (Sec. IV E). The spatial heterogeneity in the
 448 degree of thermodynamic equilibrium implies that the gas fingers are subjected to different

449 levels of dissolution/expansion effects throughout the domain. As a result, the final fingering
 450 pattern we observe is a result of the complex nonlinear coupling between hydrodynamic
 451 instabilities and thermodynamic effects. Through additional simulations in Sec. IV F, we
 452 show that both Ch and Ma can affect the fingering pattern. As Ch increases, the system
 453 experiences increasing surface tension and more pinch-off events. As Ma increases, the
 454 system takes longer to reach compositional equilibrium and the liquid composition appears
 455 more heterogeneous. Further, because a larger Ma also indirectly promotes the strength
 456 of surface tension, we also observe more tip-splitting and pinch-off events at larger Ma .
 457 Such nonlinear coupling between fingering instability and dissolution effects results in a
 458 non-monotonic trend in mixing efficiency as a function of Ma .

459 An important assumption we make in this paper is that the thermodynamic-driven com-
 460 ponent exchange does not change the density or viscosity of either fluid, or the interfacial
 461 tension between the two phases. This assumption allows us to simplify the parameter space
 462 for our simulations and thus focus on the effect of viscosity contrast and initial fluid com-
 463 positions. However, these assumptions may no longer be valid for realistic fluid pairs where
 464 density, viscosity and interfacial tension can change appreciably due to mass transfer across
 465 phases. As explained in Sec. IV G, our current model does not reproduce miscible viscous
 466 fingering pattern as we close the miscibility gap; surface tension plays a significant role in
 467 the fingering instability for all values of fluid miscibility gap in our model. We attribute
 468 this to an oversimplified design of viscosity and surface tension, which we plan to extend
 469 in future work. Further, the effect of component exchange on fluid properties could yield
 470 interesting displacement dynamics. For instance, while we only explore the displacement dy-
 471 namics under a viscously unstable configuration ($R > 0$) in this work, unstable displacement
 472 could still arise under an initially viscously stable configuration ($R < 0$). Under constant
 473 fluid-fluid component exchange, this instability could be caused by, for example, nonuni-
 474 form changes in local surface tension at the fluid interface (a Marangoni effect) or changes
 475 in local fluid viscosity that eventually reverse the viscosity contrast. It would be interesting
 476 to incorporate these effects in our current model in the future to fully understand ongoing
 477 experimental studies [28].

-
- 478 [1] P. G. Saffman and G. I. Taylor, “The penetration of a fluid into a porous medium or Hele-Shaw
479 cell containing a more viscous liquid,” *Proc. R. Soc. A* **245**, 1242 (1958).
- 480 [2] G. M. Homsy, “Viscous fingering in porous media,” *Annu. Rev. Fluid Mech.* **19**, 271–311
481 (1987).
- 482 [3] J.-D. Chen, “Fingering in Hele-Shaw cells,” *Exp. Fluids* **5**, 363–371 (1987).
- 483 [4] L. Paterson, “Radial fingering in a Hele-Shaw cell,” *J. Fluid Mech.* **113**, 513–529 (1981).
- 484 [5] J.-D. Chen, “Growth of radial viscous fingers in a Hele-Shaw cell,” *J. Fluid Mech.* **201**, 223–242
485 (1989).
- 486 [6] I. Bischofberger, R. Ramachandran, and S. R. Nagel, “Fingering versus stability in the limit
487 of zero interfacial tension,” *Nat. Comm.* **5**, 5265 (2014).
- 488 [7] J. Y.-Y. Chui, P. de Anna, and R. Juanes, “Interface evolution during radial miscible viscous
489 fingering,” *Phys. Rev. E* **92**, 041003 (2015).
- 490 [8] C. T. Tan and G. M. Homsy, “Simulation of nonlinear viscous fingering in miscible displace-
491 ment,” *Phys. Fluids* **6**, 1330–1338 (1988).
- 492 [9] C.-Y. Chen and E. Meiburg, “Miscible porous media displacements in the quarter five-spot
493 configuration. Part 1. The homogeneous case,” *J. Fluid Mech.* **371**, 233–268 (1998).
- 494 [10] A. Riaz and E. Meiburg, “Three-dimensional miscible displacement simulations in homoge-
495 neous porous media with gravity override,” *J. Fluid Mech.* **494**, 95–117 (2003).
- 496 [11] B. Jha, L. Cueto-Felgueroso, and R. Juanes, “Fluid mixing from viscous fingering,” *Phys.*
497 *Rev. Lett.* **106**, 194502 (2011).
- 498 [12] B. Jha, L. Cueto-Felgueroso, and R. Juanes, “Synergetic fluid mixing from viscous fingering
499 and alternating injection,” *Phys. Rev. Lett.* **111**, 144501 (2013).
- 500 [13] E. Lajeunesse, J. Martin, N. Rakotomalala, and D. Salin, “3D instability of miscible displace-
501 ments in a Hele-Shaw cell,” *Phys. Rev. Lett.* **79**, 5254–5257 (1997).
- 502 [14] C.-Y. Chen, L. Wang, and E. Meiburg, “Miscible droplets in a porous medium and the effects
503 of Korteweg stresses,” *Phys. Fluids* **13**, 2447–2456 (2001).
- 504 [15] C.-Y. Chen and E. Meiburg, “Miscible displacements in capillary tubes: Influence of Korteweg
505 stresses and divergence effects,” *Phys. Fluids* **14**, 2052–2058 (2002).
- 506 [16] S. Swernath, B. Malengier, and S. Pushpavanam, “Effect of Korteweg stress on viscous

- 507 fingering of solute plugs in a porous medium,” *Chem. Eng. Sci.* **65**, 2284–2291 (2010).
- 508 [17] D. Truzzolillo, S. Mora, C. Dupas, and L. Cipelletti, “Off-equilibrium surface tension in
509 colloidal suspensions,” *Phys. Rev. Lett.* **112** (2013).
- 510 [18] W. Henry, “Experiments on the quantity of gases absorbed by water, at different temperatures,
511 and under different pressures,” *Phil. Trans. R. Soc. A* **93**, 29–42 (1803).
- 512 [19] F. M. Orr, *Theory of Gas Injection Processes* (Tie-Line Publications, 2007).
- 513 [20] S. Li, J. S. Lowengrub, J. Fontana, and P. Palffy-Muhoray, “Control of viscous fingering
514 patterns in a radial Hele-Shaw cell,” *Phys. Rev. Lett.* **102**, 174501 (2009).
- 515 [21] C.-Y. Chen, C. W. Huang, L. C. Wang, and J. A. Miranda, “Controlling radial fingering
516 patterns in miscible confined flows,” *Phys. Rev. E* **82**, 056308 (2010).
- 517 [22] T. T. Al-Housseiny, P. A. Tsai, and H. A. Stone, “Control of interfacial instabilities using
518 flow geometry,” *Nat. Phys.* **8**, 747–750 (2012).
- 519 [23] D. Pihler-Puzović, P. Illien, M. Heil, and A. Juel, “Suppression of complex finger-like patterns
520 at the interface between air and a viscous fluid by elastic membranes,” *Phys. Rev. Lett.* **108**,
521 074502 (2012).
- 522 [24] Y. Nagatsu, Y. Ishii, Y. Tada, and A. De Wit, “Hydrodynamic fingering instability induced
523 by a precipitation reaction,” *Phys. Rev. Lett.* **113**, 024502 (2014).
- 524 [25] T. J. Ober, D. Foresti, and J. A. Lewis, “Active mixing of complex fluids at the microscale,”
525 *Proc. Natl. Acad. Sci. U.S.A.* **112**, 12293–12298 (2015).
- 526 [26] C. P. Brangwynne, P. Tompa, and R. V. Pappu, “Polymer physics of intracellular phase
527 transitions,” *Nat. Phys.* **11**, 899–904 (2015).
- 528 [27] M. J. Martinez and M. A. Hesse, “Two-phase convective CO₂ dissolution in saline aquifers,”
529 *Water Resour. Res.* **52**, 585–599 (2016).
- 530 [28] R. Suzuki, Y. Nagatsu, M. Mishra, and T. Ban, “Experimental study on viscous fingering with
531 partial miscible fluids,” (2016), 69th Annual Meeting of the APS Division of Fluid Dynamics.
- 532 [29] C.-Y. Chen and P.-Y. Yan, “A diffuse interface approach to injection-driven flow of different
533 miscibility in heterogeneous porous media,” *Phys. Fluids* **27**, 083101 (2015).
- 534 [30] J. W. Cahn and J. E. Hilliard, “Free energy of a nonuniform system. I. Interfacial free energy,”
535 *J. Chem. Phys.* **28**, 258 (1958).
- 536 [31] G. Tryggvason and H. Aref, “Numerical experiments on Hele-Shaw flow with a sharp inter-
537 face,” *J. Fluid Mech.* **136**, 1–30 (1983).

- 538 [32] E. Meiburg and G. M. Homsy, “Nonlinear unstable viscous fingers in Hele-Shaw flows. II.
539 Numerical simulation,” *Phys. Fluids* **31**, 429 (1988).
- 540 [33] A. Lindner, D. Bonn, E. Poiré Corvera, M. Ben Amar, and J. Meunier, “Viscous fingering in
541 non-Newtonian fluids,” *J. Fluid Mech.* **469**, 237–256 (2002).
- 542 [34] S. Nguyen, R. Folch, V. K. Verma, H. Henry, and M. Plapp, “Phase-field simulations of
543 viscous fingering in shear-thinning fluids,” *Phys. Fluids* **22**, 103102 (2010).
- 544 [35] L. Cueto-Felgueroso and R. Juanes, “Macroscopic phase-field model of partial wetting: bubbles
545 in a capillary tube,” *Phys. Rev. Lett.* **108**, 144502 (2012).
- 546 [36] L. Cueto-Felgueroso and R. Juanes, “A phase-field model of two-phase Hele-Shaw flow,” *J.*
547 *Fluid Mech.* **758**, 522–552 (2014).
- 548 [37] P. Petitjeans and T. Maxworthy, “Miscible displacements in capillary tubes. Part 1. Experi-
549 ments,” *J. Fluid Mech.* **326**, 37–56 (1996).
- 550 [38] C. Y. Chen and E. Meiburg, “Miscible displacements in capillary tubes. Part 2. Numerical
551 simulations,” *J. Fluid Mech.* **326**, 57–90 (1996).
- 552 [39] Z. Yang and Y. C. Yortsos, “Asymptotic solutions of miscible displacements in geometries of
553 large aspect ratio,” *Phys. Fluids* **9**, 286–298 (1997).
- 554 [40] A. Aubertin, G. Gauthier, J. Martin, D. Salin, and L. Talon, “Miscible viscous fingering in
555 microgravity,” *Phys. Fluids* **21**, 054107 (2009).
- 556 [41] R. M. Oliveira and E. Meiburg, “Miscible displacements in Hele-Shaw cells: three-dimensional
557 Navier–Stokes simulations,” *J. Fluid Mech.* **687**, 431–460 (2011).
- 558 [42] R. M. Oliveira and E. Meiburg, “Saffman–Taylor instability and the inner splitting mecha-
559 nism,” *Phys. Rev. Lett.* **118**, 124502 (2017).
- 560 [43] P. Aussillous and D. Quéré, “Quick deposition of a fluid on the wall of a tube,” *Phys. Fluids*
561 **12**, 2367–2371 (2000).
- 562 [44] B. Levaché and D. Bartolo, “Revisiting the Saffman-Taylor experiment: imbibition patterns
563 and liquid-entrainment transitions,” *Phys. Rev. Lett.* **113**, 044501 (2014).
- 564 [45] B. Zhao, C. W. MacMinn, and R. Juanes, “Wettability control on multiphase flow in patterned
565 microfluidics,” *Proc. Natl. Acad. Sci. U.S.A.* **113**, 10251–10256 (2016).
- 566 [46] D. M. Anderson, G. B. McFadden, and A. A. Wheeler, “Diffuse-interface methods in fluid
567 mechanics,” *Annu. Rev. Mater. Res.* **30**, 139–165 (1998).
- 568 [47] R. Folch, J. Casademunt, A. Hernández-Machado, and L. Ramirez-Piscina, “Phase-field mod-

- 569 els for Hele-Shaw flows with arbitrary viscosity contrast. I. Theoretical approach,” *Phys. Rev.*
570 *E* **60**, 1724–1733 (1999).
- 571 [48] R. Folch, J. Casademunt, A. Hernández-Machado, and L. Ramirez-Piscina, “Phase-field mod-
572 els for Hele-Shaw flows with arbitrary viscosity contrast. II. Numerical study,” *Phys. Rev. E*
573 **60**, 1734–1740 (1999).
- 574 [49] A. Hernández-Machado, M. Lacasta, E. Mayoral, and E. Corvera-Poiré, “Phase-field model
575 of Hele-Shaw flows in the high-viscosity contrast regime,” *Phys. Rev. E* **68**, 046310 (2003).
- 576 [50] H.-G Lee, J. S. Lowengrub, and J. Goodman, “Modeling pinchoff and reconnection in a
577 Hele-Shaw cell. I. The models and their calibration,” *Phys. Fluids* **14**, 492–513 (2002).
- 578 [51] H.-G Lee, J. S. Lowengrub, and J. Goodman, “Modeling pinchoff and reconnection in a Hele-
579 Shaw cell. II. Analysis and simulation in the nonlinear regime,” *Phys. Fluids* **14**, 514–545
580 (2002).
- 581 [52] Y. Sun and C. Beckermann, “A two-phase diffuse-interface model for Hele-Shaw flows with
582 large property contrasts,” *Physica D* **237**, 3089–3098 (2008).
- 583 [53] L. Cueto-Felgueroso and R. Juanes, “Nonlocal interface dynamics and pattern formation in
584 gravity-driven unsaturated flow through porous media,” *Phys. Rev. Lett.* **101**, 244504 (2008).
- 585 [54] X. Fu, L. Cueto-Felgueroso, and R. Juanes, “Thermodynamic coarsening arrested by viscous
586 fingering in partial-miscible binary mixtures,” *Phys. Rev. E* **94**, 033111 (2016).
- 587 [55] R. Ruiz and D. Nelson, “Turbulence in binary fluid mixtures,” *Phys. Rev. A* **23**, 6 (1981).
- 588 [56] A. J. Wagner and J. M. Yeomans, “Breakdown of scale-invariance in the coarsening of phase-
589 separating binary fluids,” *Phys. Rev. Lett.* **80**, 1429–1432 (1998).
- 590 [57] Z. Shou and A. Chakrabarti, “Ordering of viscous liquid mixtures under a steady shear flow,”
591 *Phys. Rev. E* **61**, 2200–2203 (2000).
- 592 [58] L. Berthier, J.-L. Barrat, and J. Kurchan, “Phase separation in a chaotic flow,” *Phys. Rev.*
593 *Lett.* **86**, 2014–2017 (2001).
- 594 [59] S. Berti, G. Boffetta, M. Cencini, and A. Vulpiani, “Turbulence and coarsening in active and
595 passive binary mixtures,” *Phys. Rev. Lett.* **95**, 224501 (2005).
- 596 [60] P. Perlekar, R. Benzi, H. J. H. Clercx, D. R. Nelson, and F. Toschi, “Spinodal decomposition
597 in homogeneous and isotropic turbulence,” *Phys. Rev. Lett.* **112**, 014502 (2014).
- 598 [61] W. J. Boettinger, J. A. Warren, C. Beckermann, and A. Karma, “Phase-field simulation of
599 solidification,” *Annu. Rev. Mater. Res.* **32**, 163–194 (2002).

- 600 [62] P. Hohenberg and B. Halperin, “Theory of dynamic critical phenomena,” *Rev. Mod. Phys.* **49**,
601 435–479 (1977).
- 602 [63] S. M. Allen and J. W. Cahn, “A microscopic theory for antiphase boundary motion and its
603 application to antiphase domain coarsening,” *Acta Metall.* **27**, 1085–1095 (1979).
- 604 [64] A. A. Wheeler, W. J. Boettinger, and G. B. McFadden, “Phase-field model of solute trapping
605 during solidification,” *Phys. Rev. E* **47**, 1893–1909 (1993).
- 606 [65] G. Wilson, “A new expression for the excess free energy of mixing,” *J. Am. Chem. Soc.* **86**,
607 127–130 (1964).
- 608 [66] A. J. Bray, “Theory of phase ordering kinetics,” *Adv. Phys.* **43**, 357–459 (1995).
- 609 [67] T. P. Witelski, “The structure of internal layers for unstable nonlinear diffusion equations,”
610 *Stud. Appl. Math.* **97**, 277–300 (1996).
- 611 [68] P. A. Witherspoon and D. N. Saraf, “Diffusion of methane, ethane, propane, and n-butane,”
612 *J. Phys. Chem.* **69**, 3752–3755 (1965).
- 613 [69] A. L. Bertozzi, N. Ju, and H.-W. Lu, “A biharmonic-modified forward time stepping method
614 for fourth order nonlinear diffusion equations,” *J. Discrete Continuous Dyn. Syst.* **29**, 1367–
615 1391 (2011).
- 616 [70] T. Maxworthy, “Bubble formation, motion and interaction in a Hele-Shaw cell,” *J. Fluid Mech.*
617 **173**, 95–114 (1986).
- 618 [71] J. V. Maher, “Development of viscous fingering patterns,” *Phys. Rev. Lett.* **54**, 1498–1501
619 (1985).
- 620 [72] C. W. Park and G. M. Homsy, “The instability of long fingers in Hele-Shaw flows,” *Phys.*
621 *Fluids* **28**, 1583 (1985).
- 622 [73] A. Arnéodo, Y. Couder, G. Grasseau, V. Hakim, and M. Rabaud, “Uncovering the analytical
623 Saffman-Taylor finger in unstable viscous fingering and diffusion-limited aggregation,” *Phys.*
624 *Rev. Lett.* **63**, 984–987 (1989).
- 625 [74] G. Daccord and R. Lenormand, “Fractal patterns from chemical dissolution,” *Nature* **325**,
626 41–43 (1987).
- 627 [75] A. De Wit, “Fingering of chemical fronts in porous media,” *Phys. Rev. Lett.* **87**, 054502
628 (2001).
- 629 [76] P. Szymczak and A. J. C. Ladd, “The initial stages of cave formation: Beyond the one-
630 dimensional paradigm,” *Earth Planet. Sci. Lett* **301**, 424–432 (2011).

- 631 [77] F. Haudin, J. H. E. Cartwright, F. Brau, and A. De Wit, “Spiral precipitation patterns in
632 confined chemical gardens,” *Proc. Natl. Acad. Sci. U.S.A.* **111**, 17363–17367 (2014).
- 633 [78] E. O. Dias, E. Alvarez-Lacalle, M. S. Carvalho, and J. A. Miranda, “Minimization of viscous
634 fluid fingering: A variational scheme for optimal flow rates,” *Phys. Rev. Lett.* **109**, 144502
635 (2012).
- 636 [79] H. Zhao, J. Casademunt, C. Yeung, and J. V. Maher, “Perturbing Hele-Shaw flow with a
637 small gap gradient,” *Phys. Rev. A* **45**, 2455–2462 (1992).